Supporting Information for

Beyond Crease Geometry: Multistability in Origami-Inspired Structures through Local Fold Architectures

Sagi Senderovich, Ezra Ben-Abu, Shai Elbaz, Nadav Zemah, Anna Zigelman, Amir D. Gat

Amir D. Gat.
E-mail: amirgat@technion.ac.il

S1. Fully Bistable MFT – Design and Fabrication

We fabricate the fully bistable MFT variation by fused deposition modeling (FDM) of individual thermoplastic polyurethane MFT elements (Fig. S1.A), which are then adhesively bonded into multi-module assemblies (Fig. S1.B).

Since FDM prints are prone to interlayer shear failure due to limited adhesion, we use slender hinges to bias deformation toward bending, reducing interlayer shear and improving fatigue resistance. To facilitate shape morphing, kinematic constraints are relaxed by the introduction of relief creases.

S2. Contact Constraints

The no-penetration condition is imposed on the boundary elongations of each BiPlan. For a boundary point k, the scalar gap variable is taken as the boundary elongation $w_{\partial,k}$, so that penetration corresponds to $w_{\partial,k} < 0$. Introducing the contact Lagrange multiplier $\lambda_{\partial,k}$, unilateral contact is written as the complementarity condition

$$w_{\partial,k} \geq 0, \qquad \lambda_{\partial,k} \geq 0, \qquad w_{\partial,k}\lambda_{\partial,k} = 0. \tag{1}$$

Thus, either the boundary is open, $w_{\partial,k} > 0$, and the contact force vanishes, or contact is active, $w_{\partial,k} = 0$, and the multiplier prevents penetration. This complementarity condition is regularized using the smoothed Fischer–Burmeister function:

$$\phi_{\mathrm{SFB},k}\left(w_{\partial,k}, \lambda_{\partial,k}\right) = \sqrt{w_{\partial,k}^2 + \lambda_{\partial,k}^2 + \varepsilon^2} - \left(w_{\partial,k} + \lambda_{\partial,k}\right), \tag{2}$$

where ε is a small smoothing parameter. Collecting all active boundary contact conditions yields

$$\boldsymbol{\phi}_{\mathrm{SFB}}\left(\boldsymbol{w}_\partial, \boldsymbol{\lambda}_\partial\right) = \mathbf{0}. \tag{3}$$

S3. Euler-Lagrange Governing Equations

To incorporate inertia, the kinetic energy T of the associated module is incorporated as

$$\begin{aligned} T(\boldsymbol{q}, \dot{\boldsymbol{q}}) &= \frac{1}{2}\dot{\boldsymbol{q}}^{\mathrm{T}}\boldsymbol{M}(\boldsymbol{q})\dot{\boldsymbol{q}}, \\ \boldsymbol{M}(\boldsymbol{q}) &= \int_{\mathcal{M}} \mu\left(\partial_{\boldsymbol{q}}\boldsymbol{r}\right)^{\mathrm{T}}\left(\partial_{\boldsymbol{q}}\boldsymbol{r}\right)\, dA, \end{aligned} \tag{4}$$

where $\mathcal{M}$ denotes the shell surface, μ is the surface density, and $\boldsymbol{r} = \boldsymbol{r}(\boldsymbol{r}_0; \boldsymbol{q})$ is the position of a material point $\boldsymbol{r}_0$. Along with the augmented strain energy, these terms produce the module's augmented Lagrangian

$$\mathcal{L}_{\mathrm{aug}} = T - \Pi_{\mathrm{aug}}. \tag{5}$$

Thus, we obtain each substructure's Euler-Lagrange governing equations and constraints:

$$\begin{gathered} \frac{d}{dt}\left(\partial_{\dot{\boldsymbol{\eta}}}\mathcal{L}_{\mathrm{aug}}\right) - \partial_{\boldsymbol{\eta}}\mathcal{L}_{\mathrm{aug}} = \partial_{\boldsymbol{\eta}}W_{\mathrm{ext}}, \\ \boldsymbol{\phi}_{\mathrm{SFB}}(\boldsymbol{w}_\partial, \boldsymbol{\lambda}_\partial) = \mathbf{0}, \end{gathered} \tag{6}$$

where $\boldsymbol{\eta}^{\mathrm{T}} = \left[\boldsymbol{q}^{\mathrm{T}}, \boldsymbol{\lambda}^{\mathrm{T}}\right]$, and external work $W_{\mathrm{ext}} = W_{\mathrm{ext}}\left(\mathbf{q}\right)$.

S4. Numerical solver

The quasi-static response of an MFT under prescribed loading and boundary conditions is computed using an incremental Gauss–Newton scheme, whereas its dynamic response under prescribed initial and boundary conditions is obtained using an implicit Newton-based time-integration scheme. Both procedures are summarized in Fig. S2.

As shown in Fig. S2, the computational procedure consists of a driver and separate quasi-static and dynamic solvers. The driver defines the global conditions and solution regime, then invokes the quasi-static solver to compute a relaxed reference configuration $\boldsymbol{q}_{\mathrm{ref}}$. During this reference solve, the MFT is subject only to the clamped-base condition. The prescribed loads and constraints are then activated, and the driver calls the appropriate solver to compute the constrained response.

Within the quasi-static solver (Fig. S2.B), the loading interval is discretized into steps. Each step is initialized from the previously converged equilibrium, after which the prescribed loads and constraints are evaluated and the global residual is assembled from the local governing equations. The resulting augmented nonlinear algebraic system is solved iteratively for the generalized coordinates and Lagrange multipliers. Convergence is declared when the prescribed residual and step-size tolerances are satisfied. The converged configuration is then reconstructed in the global frame and stored together with its energy terms before advancing to the next step. Once the sweep is complete, the solution history is returned to the driver for post-processing.

Within the dynamic solver (Fig. S2.C), the response is evaluated at prescribed output times, beginning from the reference configuration $\boldsymbol{q}_{\mathrm{ref}}$. At each step, the loads and constraints are updated and the equations of motion are advanced implicitly from the preceding state using a Newton-based time-integration scheme. The resulting configuration is reconstructed in the global frame and stored together with its energy terms. This procedure is repeated over the prescribed time interval, after which the complete response history is returned to the driver for post-processing.

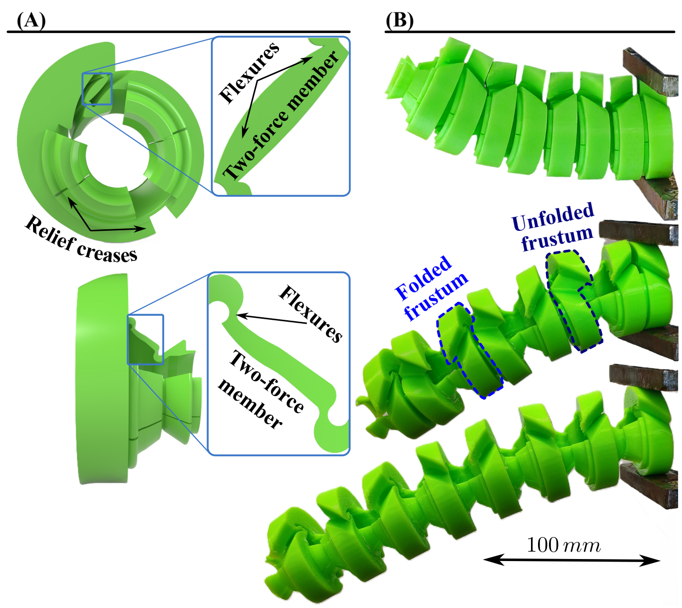

Fig. S1. A fully bistable, flexure-based MFT. (A) Front (top) and side (bottom) views of a fully bistable MFT element, with close-ups of the bistable folds (right). (B) Representative deformation modes of a flexure-based, 3D-printed MFT, with highlighted frustum states.

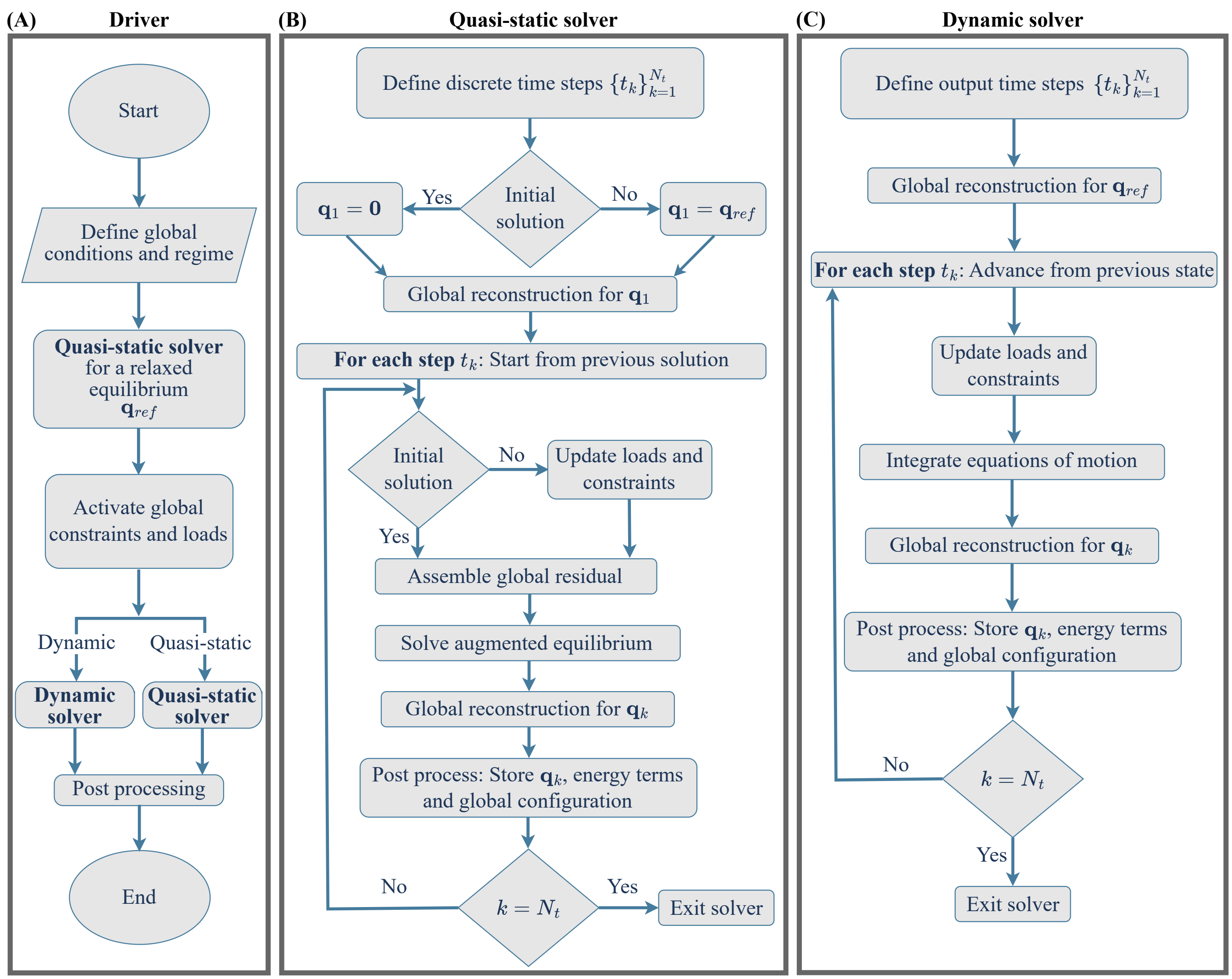

Fig. S2. Numerical solution scheme for an MFT under prescribed boundary conditions. (A) The driver defines the global conditions and solution regime, initializes a relaxed reference configuration, activates the prescribed loads and constraints, and post-processes the stored solution. (B) The quasi-static solver incrementally updates the loads and constraints, assembles the global residual, solves the augmented equilibrium system, and reconstructs the converged configuration at each step. (C) The dynamic solver advances the previous state by updating the loads and constraints and implicitly integrating the equations of motion, after which the global configuration is reconstructed and stored at each output time.

S5. Kinematics and Kinetics

A. Mixed folded tube module. We begin by constructing the kinematic mapping of each rigid element comprising the MFT module within the planar domain. First we define rotation and translation matrices

$$\mathbf{R}(\varphi) = \begin{bmatrix} \cos\varphi & -\sin\varphi \\ \sin\varphi & \cos\varphi \end{bmatrix}, \quad \mathbf{t}(\Delta z) = \begin{bmatrix} \Delta z \\ 0 \end{bmatrix}, \tag{7}$$

respectively, and an arbitrary material point's initial location vector

$$\mathbf{r}_0^T = [z_0,\, s_0]\,. \tag{8}$$

In particular, $\mathbf{r}_{0,\varphi_i}$ denotes the rotation-center location vector for element i, located at nodes A and G for $i=1$ and $i=2$, respectively (Fig. 2.C in the main text). The resulting rigid-body mapping is

$$\boldsymbol{\chi}_i(\mathbf{q}_i, \mathbf{r}_0) = \mathbf{R}(\varphi_i)\big(\mathbf{r}_0 - \mathbf{r}_{0,\varphi_i}\big) + \mathbf{t}(u), \quad i \in \{1,2\}. \tag{9}$$

We apply the established mapping to describe the MFT module's crease elongation $w(x)$. Since the module's elements are restricted to rigid-body motions, $w(x)$ varies linearly and is therefore fully determined by its boundary values. Accordingly, we compute the relative displacements of the endpoint node pairs (D,E) and (C,F), project them onto the crease axis, and interpolate the resulting boundary values to obtain $w(x)$. To this end, we define the relative-displacement operator

$$\boldsymbol{\Delta}_\partial = \begin{bmatrix} \boldsymbol{\delta}_{DE}^T \\ \boldsymbol{\delta}_{CF}^T \end{bmatrix}, \qquad \boldsymbol{\delta}_{DE} = \boldsymbol{r}_D - \boldsymbol{r}_E, \quad \boldsymbol{\delta}_{CF} = \boldsymbol{r}_C - \boldsymbol{r}_F, \tag{10}$$

where the current position of any node a associated with element i is

$$\boldsymbol{r}_a = \boldsymbol{\chi}_i(\mathbf{q}_i, \boldsymbol{r}_{a,0}), \quad i \in \{1,2\}. \tag{11}$$

The corresponding boundary elongations are obtained by projecting the endpoint relative displacements onto the helical crease axis $\boldsymbol{n}_{sp}$:

$$\boldsymbol{w}_\partial = \boldsymbol{\Delta}_\partial \boldsymbol{n}_{sp}, \quad \boldsymbol{n}_{sp}^T = [-\sin\beta,\, \cos\beta], \tag{12}$$

where the mirrored configuration is obtained by reversing the axis direction, $\boldsymbol{n}_{sp} \mapsto -\boldsymbol{n}_{sp}$. With $\boldsymbol{w}_\partial^T =: [w_0,\, w_a]$, crease elongation along the axis $x \in [0,a]$ is given by the linear interpolation

$$w(x) = \left(1 - \frac{x}{a}\right) w_0 + \frac{x}{a}\, w_a, \quad x \in [0,\, a], \tag{13}$$

where $a = l/\cos\beta$. Thus, the module's corresponding potential energy is

$$\Pi_{\text{helic}} = \int_0^a \Psi\left(w(x)\right) dx, \tag{14}$$

where Ψ represents the bistable energy density (Eq. 3 in the main text).

B. Circular crease connector. The single-pair connector (SPC) and the two-pair connector (TPC) between adjacent MFT modules m and n are parametrized by the interface displacements $\gamma_{\text{SPC}}^{(n)}$ and $\gamma_{\text{TPC}}^{(n)}$, and by the rotational generalized coordinates $\varphi_\ell^{(m)}$ and $\varphi_\ell^{(n)}$, with $\ell = 1$ for the SPC and $\ell \in \{1,2\}$ for the TPC (Figs. 2.D-E in the main text). The SPC forms an open kinematic chain and is therefore determined by the configuration of a single neighboring module relative to the connector's local reference configuration. By contrast, the TPC forms a closed kinematic chain, so its elongation is dictated by the relative motion of both modules:

$$w(x_\ell) = \begin{cases} \gamma_{\text{SPC}}^{(n)} - x_\ell \tan\!\big(\varphi_1^{(n)}\big), & \text{SPC},\ x_\ell \in [0,H],\ \ell = 1, \\ \gamma_{\text{TPC}}^{(n)} + x_\ell \Big[\tan\!\big(\varphi_\ell^{(n)}\big) - \tan\!\big(\varphi_\ell^{(m)}\big)\Big], & \text{TPC},\ x_\ell \in [0,H_\ell],\ \ell \in \{1,2\}, \end{cases} \tag{15}$$

where $H_2 = l\tan\beta$ and $H_1 = H - H_2$. Thus, the connectors' corresponding potential energy is

$$\Pi_{\text{con}} = \begin{cases} \displaystyle\int_0^H \Psi(w(x_\ell))\, dx_\ell, & \text{SPC}, \\ \displaystyle\sum_{\ell=1}^{2} \int_0^{H_\ell} \Psi(w(x_\ell))\, dx_\ell, & \text{TPC}. \end{cases} \tag{16}$$

S6. Constrained displacements

We apply the rigid-body mapping functions Eq. (9) to express boundary conditions as algebraic constraints on the mapped nodal positions (Fig. 2.C in the main text):

$$\mathbf{r}_{\mathrm{C}} = \boldsymbol{\chi}_1(\boldsymbol{q}_1, \boldsymbol{r}_{0,C}), \quad \boldsymbol{r}_{\mathrm{F}} = \boldsymbol{\chi}_2(\boldsymbol{q}_2, \boldsymbol{r}_{0,F}), \quad \text{where } \mathbf{r_{0,C}}^T = \mathbf{r_{0,F}}^T = [l,\, H]\,, \tag{17}$$

with the corresponding constrained direction $\boldsymbol{n}_c^T = [\cos\beta,\, \sin\beta]$ in the standard configuration and by $-\mathbf{n}_c$ in the mirrored configuration. We project the displacements of nodes C and F onto the constraint direction to obtain the scalar constraint measures

$$g_C = (\mathbf{r}_C - \mathbf{r}_{0,C}) \cdot \boldsymbol{n}_c, \qquad g_F = (\mathbf{r}_F - \mathbf{r}_{0,F}) \cdot \boldsymbol{n}_c, \tag{18}$$

which are enforced using Lagrange multipliers, while the compatibility constraints at nodes A and G are naturally satisfied by the mapping functions.

S7. Contact Constraints

The SFB regularization Eq. (2) is applied to the boundary elongations of the representative MFT substructures. For the MFT module, no-penetration between rigid elements is enforced at the two endpoints of the helical BiPlan (Fig. 2.C in the main text). Using the boundary elongation vector $\boldsymbol{w}_\partial$ defined in Eq. (12), the module's contact conditions are

$$\boldsymbol{\phi}^{\mathrm{mft}}_{\mathrm{SFB}}\left(\boldsymbol{w}_\partial, \boldsymbol{\lambda}_\partial\right) = \mathbf{0}. \tag{19}$$

For the circular-crease connectors, no-penetration is enforced through the most restrictive boundary elongation over the connector BiPlans:

$$\phi^{\mathrm{con}}_{\mathrm{SFB}}\left(w_\partial, \lambda_\partial\right) = 0, \quad w_\partial = \min_{\ell,\, x_\ell \in \partial\Omega_\ell} w_\ell(x_\ell), \tag{20}$$

where ℓ indexes the connector BiPlans and $\partial\Omega_\ell$ denotes their boundary points.

S8. Global Reconstruction

We consider a sequence of N MFT modules, indexed by $m \in \{1, \ldots, N\}$, and their connecting interfaces. Each module contains n nodes and is parameterized by the generalized-coordinate vectors

$$\mathbf{q}_i^{(m)} = [u_m,\, \varphi_i^{(m)}]^{\mathrm{T}}, \quad i \in \{1, 2\}, \tag{21}$$

together with the interface displacements γ_m, where interface m connects modules $k = m - 1$ and m (Figs. 2.C-E in the main text). For each module m, the local rigid-body mapping Eq. (9) yield the nodal position matrix $\mathbf{X}^{(m)}(\mathbf{q}^{(m)}) \in \mathbb{R}^{2\times n}$ in the (z, s) plane, whose jth column $\mathbf{X}_j^{(m)}$ provides the position of node j. The full sequence is reconstructed by assembling the local module configurations through chain kinematics.

While TPCs introduce a locally closed kinematic loop, SPCs form an open chain in which rotations and deflections propagate to downstream modules. We therefore employ dedicated kinematic operators for each connector type. For adjacent modules k and m, the SPC relative motion is represented by a rotation $\theta_m = \varphi_1^{(k)}$ about the pivot point $\mathbf{p}_m = \mathbf{X}_1^{(k)}$, yielding the homogeneous rigid-body transforms

$$\mathbf{H}_m^{\mathrm{SPC}} = \begin{bmatrix} \mathbf{R}(\theta_m) & \mathbf{p}_m - \mathbf{R}(\theta_m)\mathbf{p}_m \\ \mathbf{0} & 1 \end{bmatrix}, \quad \mathbf{H}_m^{\mathrm{TPC}} = \mathbf{I}_3, \tag{22}$$

where $\mathbf{H}_m \in \left\{\mathbf{H}_m^{\mathrm{SPC}},\, \mathbf{H}_m^{\mathrm{TPC}}\right\}$ denotes the operator associated with the connector type under consideration. The corresponding translation vector is

$$\boldsymbol{a}_m = \Delta_m \cdot \left[1,\, c_m\right]^T, \tag{23}$$

where

$$\Delta_m = \gamma_m - u_m + l, \quad c_m = \begin{cases} \tan\theta_m, & \text{SPC}, \\ 0, & \text{TPC}. \end{cases} \tag{24}$$

The relative homogeneous transform from module m to the adjacent upstream module k is therefore

$$\mathbf{T}_m = \begin{bmatrix} \mathbf{I}_2 & \boldsymbol{a}_m \\ \mathbf{0}^T & 1 \end{bmatrix} \mathbf{H}_m \in \mathbb{R}^{3\times 3}, \tag{25}$$

with $m \in \{2, \ldots, N\}$ and $\mathbf{T}_1 = \mathbf{I}$. Thus, the absolute placement of module m in the global frame is obtained by the standard serial product

$$^0\mathbf{T}_m = \prod_{j=2}^{m} \mathbf{T}_j, \quad ^0\mathbf{T}_1 = \mathbf{I}. \tag{26}$$

Using the global transform matrix, we lift the local node matrix to homogeneous form:

$$\tilde{\mathbf{X}}^{(m)} = \begin{bmatrix} \mathbf{X}^{(m)} \\ \mathbf{1}^T \end{bmatrix} \in \mathbb{R}^{3\times n}, \tag{27}$$

and obtain the global homogeneous node coordinates from the single matrix product

$$\bar{\mathbf{X}}^m = {}^0\mathbf{T}_m \, \tilde{\mathbf{X}}^{(m)}. \tag{28}$$

Having established the global reconstruction procedure, the external loads and constraints comprising the structure's global boundary conditions can be applied in the global frame via standard virtual work and Lagrange multipliers, respectively.

S9. Semi-Bistable MFT Design Maps

The force-controlled deformation maps in Fig. 3.A.1 are obtained from the dynamic response of the semi-bistable MFT under the monotonic axial-force ramp

$$F(t) = \dot{F}t, \quad \dot{F} = 0.8\ \mathrm{N\,s^{-1}}, \quad 0 \le t \le 2\ \mathrm{s}, \tag{29}$$

corresponding to a terminal force $F_f = 1.6$ N. The reported axial and radial endpoint displacements are evaluated at terminal time. The geometric ratio b and stiffness ratio C are varied over the ranges shown in Fig. 3.A.1, while all remaining parameters are held at the values listed in Table S1. The geometric ratio b is varied through β, while H and l remain fixed. The stiffness ratio C is varied through k_{helic}, while the circular-fold constitutive law remains fixed.

The displacement-controlled stability map in Fig. 3.A.3 is computed quasi-statically at $b = 0.58$. At each prescribed displacement and stiffness ratio C, distinct equilibria are identified and classified using the constrained reduced-Hessian stability criterion described in the main text.

S10. Experimental Calibration

To validate the proposed model against the experimental response of the semi-bistable MFT, we must first calibrate its stiffness and geometric parameters using measurements from the fabricated specimen. While the geometric parameters can be measured directly, the trilinear and linear stiffness laws governing the circular and helical folds, respectively, contribute simultaneously to the MFT response and therefore cannot be identified independently from measurements of the complete structure. To isolate these contributions, we fabricate Circular Folded Tubes (CFTs) containing either trilinear or linear-stiffness folds and measure their responses under axial loads (Fig. S3).

The linear CFT is measured under pressure-driven extension. For the trilinear CFT, the first and second phases are characterized under pressure-driven extension and gravity-induced contraction, respectively, up to the stability limit of each phase. The response within the spinodal region is then interpolated between the two measured instability points.

The responses are measured across ten specimens, from which the median response is calculated together with a ± 1 standard-deviation band. The median responses are then fitted with linear functions using a least-squares approach. These fits are distributed along the folds to define the constitutive laws governing their spatially varying stiffness fields, as specified in Table S1.

S11. Construction of a State Transition Diagram for Fully Bistable MFTs

The state transition diagram presented in the main text is constructed through a BiPlan stability sweep over all possible fold-state configurations of a four-module fully bistable MFT. The MFT contains seven bistable folds, each of which may occupy either its closed or open stable branch, yielding $2^7 = 128$ binary fold-state combinations. For each combination, the local coordinates of the corresponding substructures are initialized toward the prescribed stable branches, and the resulting candidate configuration is relaxed quasi-statically using the procedure described in Sec. S4. After convergence, each fold is classified as closed or open according to the stable phase occupying the greater fraction of its length. Each converged configuration is then assessed using the constrained reduced-Hessian criterion described in the main text. Equilibria with a positive-definite reduced Hessian are retained as locally stable states, whereas unstable equilibria are discarded.

The sweep yields 34 stable equilibria, each of which is represented by a seven-bit binary sequence ordered from the MFT's free end toward its clamped base, with closed and open folds denoted by 0 and 1, respectively. A leading zero is appended to form an eight-bit sequence that can be represented by a two-digit hexadecimal label. For example, appending a leading zero to the binary sequence 0011011 yields 00011011, which corresponds to the hexadecimal label 1B (Fig. S4). Two retained stable equilibria are connected by an undirected edge when their seven-bit binary sequences have a Hamming distance of one, such that they differ in the state of a single fold. The resulting graph therefore represents single-fold adjacency between stable configurations, and an ordered sequence of connected states defines a transition pathway between selected initial and target configurations.

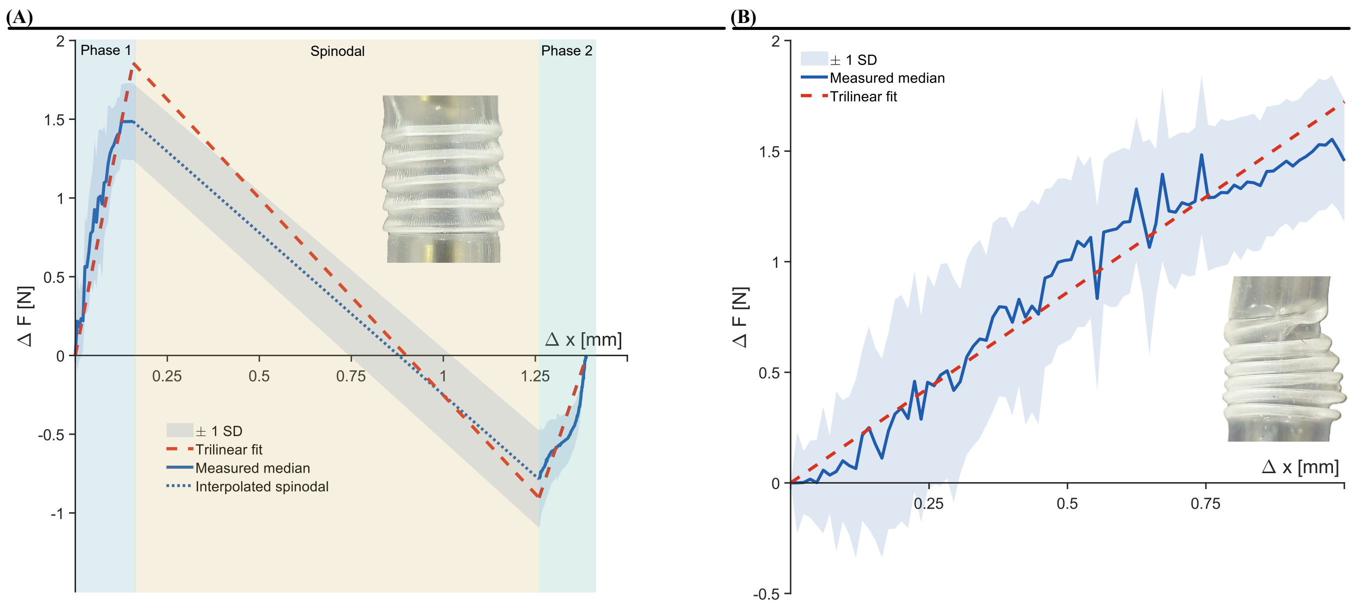

Fig. S3. Constitutive responses of Circular Folded Tubes (CFTs) incorporating (A) trilinear-stiffness folds and (B) linear-stiffness folds.

Table S1. Geometric and constitutive parameters of the validated semi-bistable MFT.

Parameter	Symbol	Value
Geometry		
Radius	R	$2.0\ \mathrm{mm}$
Module length	l	$3.6\ \mathrm{mm}$
Helical fold inclination	β	$60°$
Number of modules	N	6
Stiffness laws		
Circular-fold stiffness coefficients	$\boldsymbol{k}_{\mathrm{circ}}$	$[0.9,\ -0.2,\ 0.6]\ \mathrm{N/mm^2}$
Circular-fold transition lengths	$\boldsymbol{l}_{\mathrm{circ}}$	$[0.2,\ 1.3]\ \mathrm{mm}$
Helical-fold stiffness	k_{helic}	$1.3\ \mathrm{N/mm^2}$

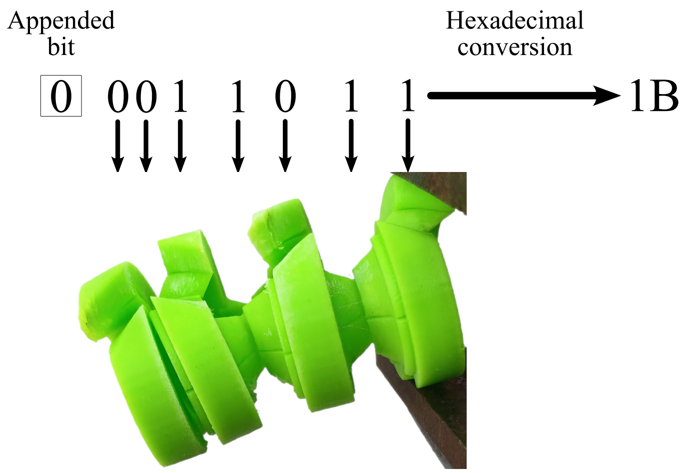

Fig. S4. Binary and hexadecimal encoding of a stable fully bistable MFT configuration. The seven fold states are ordered from the free end toward the clamped base, with closed and open folds denoted by 0 and 1, respectively. A leading zero is appended to form the eight-bit sequence 00011011, corresponding to the hexadecimal label $1\mathrm{B}$. The example shows the target configuration of pathway p_2 in the main text.

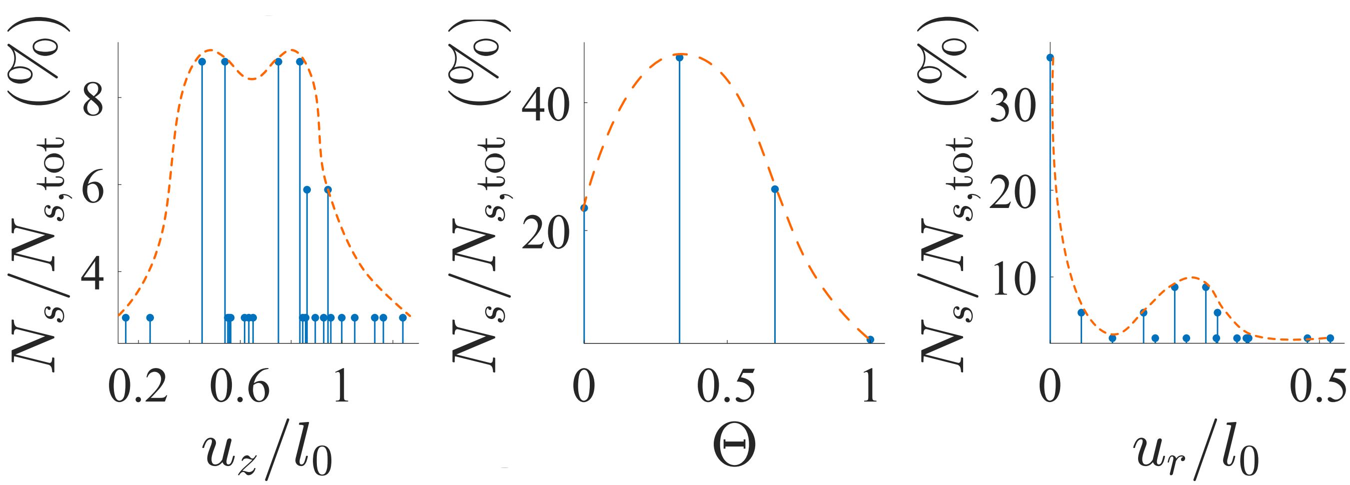

Fig. S5. Distribution of stable states within the equilibrium field and the corresponding RMS relations for endpoint deflection, elongation, and slope.

S12. Configuration-Space Hierarchy of Fully Bistable MFTs

Figure S5 reports equal-weight state-count distributions over endpoint slope, elongation, and deflection. Because most stable states contain a single open helical fold, the slope distribution is unimodal and peaks near $\Theta = 1/3$. The elongation distribution is bimodal, reflecting the iso-elongation subbranches associated with the $\Theta = 1/3$ and $\Theta = 2/3$ slope branches. The deflection distribution exhibits a dominant peak near zero, arising from purely elongational states and from states in which only the helical fold nearest the free end is open, such as the first state of pathway p_3 (Fig. 4.D in the main text). A smaller secondary peak spans $u_r/l_0 \in [1/8, 5/8]$, where configurations with one and two open helical folds produce comparable deflections under different circular-fold configurations (Fig. 4.B in the main text).

Movie S1. Experimental validation of the BiPlan framework for a pneumatically actuated six-module semi-bistable MFT. Top: modeled response in the planar development. Middle: reconstructed cylindrical response. Bottom: experimentally measured response.